

PAPER • OPEN ACCESS

A direct comparison of multi-energy x-ray and proton CT for imaging and relative stopping power estimation of plastic and *ex-vivo* phantoms

To cite this article: Elena Fogazzi *et al* 2024 *Phys. Med. Biol.* **69** 175021

View the [article online](#) for updates and enhancements.

You may also like

- [Opportunities and challenges of upright patient positioning in radiotherapy](#)
Lennart Volz, James Korte, Maria Chiara Martire *et al.*
- [Global and local feature extraction based on convolutional neural network residual learning for MR image denoising](#)
Meng Li, Juntong Yun, Dingxi Liu *et al.*
- [Modelling radiobiology](#)
Lydia L Gardner, Shannon J Thompson, John D O'Connor *et al.*

LAP

LUNA 3D
**The New More
in SGRT**

Experience safety, efficiency,
and comfort in radiation therapy

www.lap-laser.com

Availability of products, features, and services may vary depending on your location.

THETIS

DORADOnova Bridge

APOLLO

AQUARIUS

LUNA 3D

RadCalc

EASY CUBE

EASY SLAB



PAPER

OPEN ACCESS

RECEIVED
14 May 2024REVISED
8 August 2024ACCEPTED FOR PUBLICATION
19 August 2024PUBLISHED
30 August 2024

Original Content from
this work may be used
under the terms of the
[Creative Commons
Attribution 4.0 licence](#).

Any further distribution
of this work must
maintain attribution to
the author(s) and the title
of the work, journal
citation and DOI.



A direct comparison of multi-energy x-ray and proton CT for imaging and relative stopping power estimation of plastic and ex-vivo phantoms

Elena Fogazzi^{1,2,12} , Guyue Hu^{3,12} , Mara Bruzzi^{4,5}, Paolo Farace^{2,6} , Thomas Kröncke⁷, Katharina Niepel³, Jens Ricke⁸, Franka Risch⁷, Bastian Sabel⁸, Monica Scaringella⁴ , Florian Schwarz⁷, Francesco Tommasino^{1,2,*} , Guillaume Landry^{9,10,11,13} , Carlo Civinini^{4,13}  and Katia Parodi^{3,10,13} 

- ¹ Physics Department, University of Trento, Trento, TN, Italy
 - ² Trento Institute for Fundamental Physics and Applications (TIFPA), Italian National Institute of Nuclear Physics (INFN), Trento, TN, Italy
 - ³ Department of Medical Physics, Faculty of Physics, LMU Munich, Garching, Germany
 - ⁴ Italian National Institute of Nuclear Physics (INFN), Florence section, Sesto Fiorentino, FI, Italy
 - ⁵ Physics and Astronomy Department, University of Florence, Sesto Fiorentino, FI, Italy
 - ⁶ Medical Physics Unit, Hospital of Trento, Azienda Provinciale per i Servizi Sanitari (APSS), Trento, Italy
 - ⁷ Department of Diagnostic and Interventional Radiology, University Hospital Augsburg, Augsburg, Germany
 - ⁸ Department of Radiology, LMU University Hospital, LMU Munich, Munich, Germany
 - ⁹ Department of Radiation Oncology, LMU University Hospital, LMU Munich, Munich, Germany
 - ¹⁰ German Cancer Consortium (DKTK), Partner Site Munich, Munich, Germany
 - ¹¹ Bavarian Cancer Research Centre (BZKF), Munich, Germany
 - ¹² Co-first authors.
 - ¹³ Co-last authors.
- * Author to whom any correspondence should be addressed.

E-mail: francesco.tommasino@unitn.it

Keywords: proton therapy, relative stopping power, proton imaging, proton CT, photon-counting CT, dual-energy CT

Supplementary material for this article is available [online](#)

Abstract

Objective. Proton therapy administers a highly conformal dose to the tumour region, necessitating accurate prediction of the patient's 3D map of proton relative stopping power (RSP) compared to water. This remains challenging due to inaccuracies inherent in single-energy computed tomography (SECT) calibration. Recent advancements in spectral x-ray CT (xCT) and proton CT (pCT) have shown improved RSP estimation compared to traditional SECT methods. This study aims to provide the first comparison of the imaging and RSP estimation performance among dual-energy CT (DECT) and photon-counting CT (PCCT) scanners, and a pCT system prototype. **Approach.** Two phantoms were scanned with the three systems for their performance characterisation: a plastic phantom, filled with water and containing four plastic inserts and a wood insert, and a heterogeneous biological phantom, containing a formalin-stabilised bovine specimen. RSP maps were generated by converting CT numbers to RSP using a calibration based on low- and high-energy xCT images, while pCT utilised a distance-driven filtered back projection algorithm for RSP reconstruction. Spatial resolution, noise, and RSP accuracy were compared across the resulting images. **Main results.** All three systems exhibited similar spatial resolution of around 0.54 lp/mm for the plastic phantom. The PCCT images were less noisy than the DECT images at the same dose level. The lowest mean absolute percentage error (MAPE) of RSP, $(0.28 \pm 0.07)\%$, was obtained with the pCT system, compared to MAPE values of $(0.51 \pm 0.08)\%$ and $(0.80 \pm 0.08)\%$ for the DECT- and PCCT-based methods, respectively. For the biological phantom, the xCT-based methods resulted in higher RSP values in most of the voxels compared to pCT. **Significance.** The pCT system yielded the most accurate estimation of RSP values for the plastic materials, and was thus used to benchmark the xCT calibration performance on the

biological phantom. This study underlined the potential benefits and constraints of utilising such a novel *ex-vivo* phantom for inter-centre surveys in future.

1. Introduction

The highly conformal dose distribution is the most evident benefit of proton therapy compared to conventional radiotherapy. As a consequence, accurate definition of the target geometry and stopping properties is crucial at the treatment planning stage. This is typically predicted by the 3D map of the proton relative stopping power (RSP) values of the patient with respect to water. In current clinical practice, the 3D RSP map is calculated from the 3D distribution of computed tomography (CT) number (expressed in terms of Hounsfield unit, HU), obtained from imaging the patient with an x-ray CT (xCT) scan (Schneider *et al* 1996). However, the standard calibration method based on single-energy xCT (SECT) has shown range uncertainties typically up to 3.5% (Yang *et al* 2012).

Recent developments in spectral xCT imaging have provided new prospects to improve RSP estimation accuracy and thus reduce range prediction uncertainties (Li *et al* 2017, Si-Mohamed *et al* 2017, Shen *et al* 2018, Willeminck *et al* 2018, Wohlfahrt and Richter 2020). Dual-energy CT (DECT) employs information from the patient, gathered through two distinct energy spectra. More recently, commercially available photon-counting CT (PCCT) scanners enable multi-energy processing by counting individual photons in selected energy bins. Therefore, DECT and PCCT datasets allow a more accurate estimation of the relative electron density (RED) and the effective atomic number (EAN) of materials from xCT images acquired at different energies, and then the calculation of proton RSP maps. These methods based on multi-energy CT have demonstrated improved accuracy for treatment planning compared to conventional SECT-based methods in several studies (Möhler *et al* 2016, Taasti *et al* 2017, 2018b, Wohlfahrt *et al* 2017, Niepel *et al* 2021)

As an alternative, proton imaging is under continuous investigation (Johnson *et al* 2016, Pettersen *et al* 2017, Esposito *et al* 2018, Civinini *et al* 2020, DeJongh *et al* 2021b). A proton CT (pCT) scanner would allow directly mapping the 3D RSP map of the patient, using low intensity clinical proton beams which are transmitted through the patient. Different pCT prototypes have been developed, showing higher RSP accuracy than standard SECT calibrations (Bär *et al* 2022, Dedes *et al* 2022, Fogazzi *et al* 2023). However, these promising prototypes are currently in the research and development stage, and cannot be directly employed with patients in clinical settings at this time. In this context, an alternative approach has been proposed in Farace *et al* (2021) and further investigated in Fogazzi *et al* (2024). This is based on the pCT acquisition of heterogeneous, biological targets, to verify and, possibly, to correct the CT-RSP calibrations for SECT.

This study aims to perform a first comprehensive comparison between a pCT prototype and clinical DECT and PCCT systems, analysing both the imaging performances (i.e. spatial resolution and noise) and the accuracy of the RSP values on plastic as well as on heterogeneous biological targets.

2. Materials and methods

2.1. Phantoms

This study employed three phantom types: one for the calibration of xCT scanners and two for the comparative analysis between xCTs and pCT.

Firstly, a custom cylindrical PMMA phantom, with a diameter of 15 cm and a height of 28 cm, housing twelve tissue-equivalent inserts (Gammex, Inc. Middleton, WI, USA) was scanned, serving as a calibration phantom both for DECT and PCCT scanners for RSP estimation. The mass density of the Gammex inserts used for calibration ranged between 0.29 g cm^{-3} and 1.82 g cm^{-3} . Details of the mass density and elemental composition of the inserts are listed in table 1 in Hudobivnik *et al* (2016).

Secondly, a custom-built plastic phantom (figure 1(a)) was scanned to investigate the CT imaging performances (sections 2.4–5) (Fogazzi *et al* 2023). It had a cylindrical shape with 0.5 cm thick PMMA walls, 14 cm inner diameter, and 13 cm height. The phantom contained five different cylindrical inserts (3 cm diameter, 6 cm length) that, although not tissue-equivalent, resembled the mass density of different tissue types: low-density polyethylene (LDPE) (0.99 g cm^{-3}), Acrylic (1.20 g cm^{-3}), Delrin (1.41 g cm^{-3}), Teflon (2.18 g cm^{-3}), and beech wood ($\approx 0.66 \text{ g cm}^{-3}$). In particular, the latter was chosen to have a first, qualitative investigation of the pCT response to a heterogeneous material. The phantom was filled with distilled water. In this way, homogeneous slices of water could be imaged in the upper part of the phantom to measure the RSP value of water, as reference material, and the noise spectrum, as described in section 2.4.

Finally, a biological phantom (bio-phantom), consisting of an insert made from a formalin-stabilised bovine specimen, was realised and used to compare the RSP maps of biological tissues obtained with the different CT systems. The specimen was a heterogeneous anatomical section of bovine abdominal area that included visible portions of fat, muscle, and bone tissues (figure 1(e)). The histological stabilisation process utilised buffered formalin to preserve the physiological features of the tissues, as reported in Fogazzi *et al* (2024). In addition, agar-agar hydrogel was employed to embed the tissues within a rigid aqueous matrix, housed in a plastic cylinder (11 cm diameter, 8 cm length, 0.5 cm thick PMMA walls).

2.2. xCT acquisitions and calibrations

All the phantoms were scanned (i) at a SOMATOM Definition Force DECT scanner with tube voltages of 90 Vp and 150 kVp with Sn filtration and (ii) at a NAEOTOM Alpha PCCT scanner with a tube voltage of 120 kVp using a normal-resolution mode with subpixels read out in 2×2 groups. Both xCT scans were from Siemens Healthineers, Forchheim, Germany, with a collimation width of 19.2 mm and a pitch factor of 0.7.

For all the phantoms, virtual monoenergetic images (VMIs) at energies ranging from 40 keV to 190 keV in 10 keV increments were reconstructed at the PCCT scanner, with the Qr36f convolution kernel and a quantum iterative reconstruction (QIR) strength level of 2. Equivalently, the Qr36s kernel and an Advanced Modelled Iterative REconstruction (ADMIRE) strength level of 3 were used to reconstruct the low- and high-kV DECT images. The reconstruction parameters for both DECT and PCCT are listed in table 1.

For both xCT scans, the RSP maps were converted from the measured CT numbers using a calibration method relying on a pair of low- and high-energy reconstructed xCT images. First, the RED, EAN, and mean excitation energy values of the Gammex inserts were calculated from the mass densities and elemental compositions provided by the manufacturer. The RED values (ρ_e) were then calibrated against a weighted difference between the low- and the high-energy mean CT numbers (HU_L and HU_H) of the inserts (Saito 2012):

$$\rho_e = a \frac{(1 + \alpha) HU_H - \alpha HU_L}{1000} + b, \quad (1)$$

where a , b , and α are the fit parameters. Next, the ratio of EAN values of the Gammex inserts (Z_{eff}) to that of water ($Z_{\text{eff,w}}$) was fitted to the CT number and RED (Saito and Sagara 2017b):

$$\left(\frac{Z_{\text{eff}}}{Z_{\text{eff,w}}} \right)^{3.3} - 1 = \gamma_L \left(\frac{HU_L}{1000} + 1 - \rho_e \right) + \gamma_0, \quad (2)$$

where γ_L and γ_0 are the fit parameters. The theoretical EAN was calculated from the known elemental components of the inserts (Saito and Sagara 2017b):

$$Z_{\text{eff}} = \left(\frac{\sum_i w_i Z_i A_i^{3.3}}{\sum_i w_i Z_i A_i} \right)^{1/3.3}. \quad (3)$$

with w_i , Z_i , A_i the mass fraction, the atomic number and the mass number of each i th element, respectively. A linear relationship between mean excitation energy ratio and EAN ratio (to water) was fitted based on the twelve Gammex inserts. For this fit, the inserts were divided into two groups, soft-tissue and bone-tissue inserts, respectively, separated by an EAN of 8.8. The mean excitation energy values of the inserts were calculated using the Bragg additivity rule (Saito and Sagara 2017a). Subsequently, the RSP maps were calculated from the RED (ρ_e) and mean excitation energy (I) values, estimated using the calibration results, by the Bethe-Bloch formula (Saito and Sagara 2017a):

$$\text{RSP} = \rho_e \frac{\ln \frac{2m_e c^2 \beta^2}{I(1-\beta^2)} - \beta^2}{\ln \frac{2m_e c^2 \beta^2}{I_w(1-\beta^2)} - \beta^2}, \quad (4)$$

where $I_w = 78$ eV is the mean excitation energy of water (Sigmund *et al* 2009, Seltzer *et al* 2014); β is the velocity of 100 MeV protons relative to the speed of light. For DECT, the low- and high-kV images were used to estimate the RSP maps of the phantoms. For PCCT, several pairs of low- and high-energy VMIs were evaluated based on the optimal energy pair identified in a previous study (Hu *et al* 2022). Table 1 gives a summary of the imaging doses for the xCT scans in volumetric CT dose index (CTDI_{vol}).

Table 1. Imaging acquisition and reconstruction parameters of the three scanners.

		Kernel/filter	Grid	Voxel size (mm ³)	Dose
Plastic Phantom	DECT	Qr36s, 3	512 × 512	(0.50, 0.50, 1.00)	20.0 mGy
	PCCT	Qr36f, 2	512 × 512	(0.50, 0.50, 1.00)	20.0 mGy
	pCT	Hann filter	400 × 400	(0.50, 0.50, 1.00)	11.6 mGy
Bio-Phantom	DECT	Qr36s, 3	512 × 512	(0.39, 0.39, 1.00)	20.0 mGy
	PCCT	Qr36f, 2	512 × 512	(0.50, 0.50, 1.00)	20.0 mGy
	pCT	Hann filter	400 × 400	(0.50, 0.50, 1.00)	19.5 mGy

2.3. pCT system and reconstruction

The plastic and bio-phantoms were also scanned by a pCT system, directly mapping the RSP values. Details on the apparatus were described elsewhere (Civinini *et al* 2020). Summarising, the system is based on a tracker, that is four-planes of silicon micro-strips, two upstream and two downstream the phantom to measure the position and direction of each proton. The spacing between the first and second tracker planes, as well as between the third and fourth, has been established at 15 cm each. Additionally, there is a 30 cm interval between the second and third planes, where the phantom is installed. The residual energy of each proton is measured by a scintillating calorimeter made of 14 Cerium-doped Yttrium Aluminum Garnet (YAG:Ce) crystals (Scaringella *et al* 2023). The field of view of the pCT apparatus is 5×20 cm² in the plane orthogonal to the beam direction. A 211 MeV beam of the experimental line at the Trento Proton Therapy Centre (Trentino Healthcare Agency, APSS, Italy) (Tommasino *et al* 2017) was transmitted through the phantom. During acquisitions, the phantom was placed on a remotely controlled rotating platform. The image reconstruction was made using a distance-driven filtered back projection algorithm (Rit *et al* 2013), which takes into account the most likely path of each particle within the phantom material (Schulte *et al* 2008).

To properly compare the pCT-based RSP maps with the xCT-based ones, the images were reconstructed with the same voxel size (table 1). However, it is important to note an exception in the DECT images of the bio-phantom, where voxel size adjustments were made through interpolation during post-processing. The cut-off frequency of the Hann filter (Hf), available in the pCT reconstruction algorithm, was adjusted in the range $[0, 1]$, as fraction of the Nyquist's frequency. When Hann filter is omitted (Hf 0), a conventional rectangular window is applied. The effects of the filter on pCT imaging performance were investigated in Fogazzi *et al* (2023). The estimated doses during the plastic phantom and the bio-phantom acquisition were 11.6 mGy and 19.5 mGy, respectively, according to the estimation procedure described in Civinini *et al* (2017).

2.4. Imaging performances

The imaging performances of the three scanners were first investigated through the plastic phantom images, adopting the methods described in Fogazzi *et al* (2023). For convenience, we defined the x - y plane as the plane parallel to the cylinder bases, while the z direction was along the length of the cylinder.

The spatial response of the scanners was studied by exploiting the circular edges of the phantom inserts. Summarising, the edge spread function was constructed for each insert and rebinned into one tenth of the voxel size in the x - y plane as standard procedure to estimate the presampled modulation transfer function (Dobbins III *et al* 2000). The edge spread function was also averaged over nine available slices along z direction, to avoid boundary effects. Then, the spatial resolution value was extracted from the spatial frequency corresponding to 10% of the presampled modulation transfer function maximum value.

Additionally, homogeneous water slices above the inserts were analysed to estimate the noise power spectrum (NPS) of the three scanners, as typically applied for xCT scanners (Samei *et al* 2019). For each slice, nine 2.69 cm² regions of interest (ROIs) were extracted. As further described in Fogazzi *et al* (2023), for the i th ROI in a given slice, the 2D NPS was defined as

$$\text{NPS}_i(u, v) = |\text{FFT}\{I(x, y) - I_{\text{mean},i}\}|^2, \quad (5)$$

where $I(x, y)$ was the value of the pixel at position (x, y) in the i th ROI, and $I_{\text{mean},i}$ was the pixel mean value of the i th ROI, subtracted to remove DC components in the Fourier transform. The 2D NPS for the nine ROIs within a single slice were averaged and converted into 1D radial NPS. To improve the accuracy, the 1D radial NPS was averaged over the six available water slices. Integrating the 1D NPS for all non-zero frequencies, we estimated the noise variance, thus the standard deviation.

It should be noted that the dose of xCT and pCT acquisitions of the plastic phantom were different. Therefore, careful consideration must be made when comparing the noise.

2.5. RSP accuracy

As a first benchmark of the different RSP estimations, the inserts of the plastic phantom were exploited. The RSP accuracy was estimated by extracting a circular ROI for each slice, centred in each insert, with a diameter two thirds of the diameter of the insert. The mean of the values in the ROI of each i th slice ($RSP_{\text{mean},i}$) was averaged within ten slices (RSP_{mean}), to reduce statistical fluctuations. The uncertainty associated with $RSP_{\text{mean},i}$ values was the standard deviation of pixel values in the ROI of the i th slice, normalised by the square root of the number of pixels in that ROI. The uncertainty of RSP_{mean} was obtained by error propagation. Finally, for each insert, the RSP accuracy was defined as

$$RSP_{\text{acc}} (\%) = \frac{RSP_{\text{mean}} - RSP_{\text{ref}}}{RSP_{\text{ref}}} \times 100, \quad (6)$$

where RSP_{ref} was the reference value of RSP measured with a multi-layer ionisation chamber (MLIC, Giraffe, IBA) at Trento Proton Therapy Centre, as described in Fogazzi *et al* (2023) and reported in table 3. The RSP value of water was extracted from the residual area between inserts, while the reference RSP value was the one reported by NIST (NIST 2023) for liquid water at the room temperature where the pCT was performed ($\simeq 21^\circ\text{C}$).

Finally, the mean absolute percentage error (MAPE) was estimated as

$$MAPE = \frac{\sum_{j=1}^n |RSP_{\text{acc},j} (\%)|}{n} \quad (7)$$

with n the number of materials.

2.6. Bio-phantom RSP comparison

The 3D RSP maps of the bio-phantom calculated from DECT and PCCT images were compared with those measured by the pCT system. For a voxel-wise comparison, an intensity-based, 3D rigid registration was performed with Matlab® (The MathWorks, Inc, Natick, MA, USA), using pCT as reference. A specific ROI for each slice was defined to avoid agar regions. Furthermore, in order to mitigate partial volume effects resulting from potential registration discrepancies or voxel size and noise effects, the edge voxels between distinct tissues were identified using a gradient-magnitude edge detection technique and subsequently excluded from the analysis. Finally, the RSP relative difference was defined for each voxel of the biological phantom as

$$\Delta RSP (\%) = \frac{RSP_{\text{xCT}} - RSP_{\text{pCT}}}{RSP_{\text{pCT}}} \times 100, \quad (8)$$

where RSP_{xCT} and RSP_{pCT} were the xCT and pCT-based RSP values, respectively. The result was firstly visualised by direct image subtraction, slice-by-slice. To conduct a more thorough 3D analysis, the relative difference was visualised through a histogram distribution. Furthermore, RSP thresholds were used to differentiate the contribution of various anatomical components. Namely, voxels having a pCT-based RSP value in the range [0.92, 0.98] were designated as fat tissues. For the muscle and bone regions, the ranges [1.01, 1.07] and [1.20, 2.00] were applied, respectively. These values have been adjusted from Peters *et al* (2023), based on human tissue compositions (Woodard and White 1986), according to the RSP values of the phantom measured with pCT (cf supplementary materials, section 1). Intermediate RSP values were assumed to be linked to critical structures, such as red marrow and cartilage (Schaffner and Pedroni 1998, Peters *et al* 2023), or to be caused by partial volume effects resulting from noise and spatial resolution levels. For additional validation, the identified tissue ROIs underwent visual inspection to ensure that no voxels at the interfaces between tissues with significantly different densities were included in the analysis.

It is noteworthy that xCT images were acquired under comparable conditions, specifically with the phantom being removed from the refrigerator ($\simeq 4^\circ\text{C}$) about one hour before imaging. In contrast, due to experimental setup constraints, the pCT acquisition was conducted at $\simeq 21^\circ\text{C}$ with the phantom removed from the refrigerator about 24 hours before the acquisition to ensure it fully equilibrated to room temperature. However, the RSP values for the bio-phantom could be influenced by temperature conditions during acquisition. Therefore, careful consideration of temperature conditions may be necessary when comparing RSP values.

3. Results

3.1. Imaging performances

As first qualitative comparison between the images of the three scanners, no visual artefacts are detected (figure 1). Details on the order of few millimetres, such as the wood grains and residual air bubbles, are

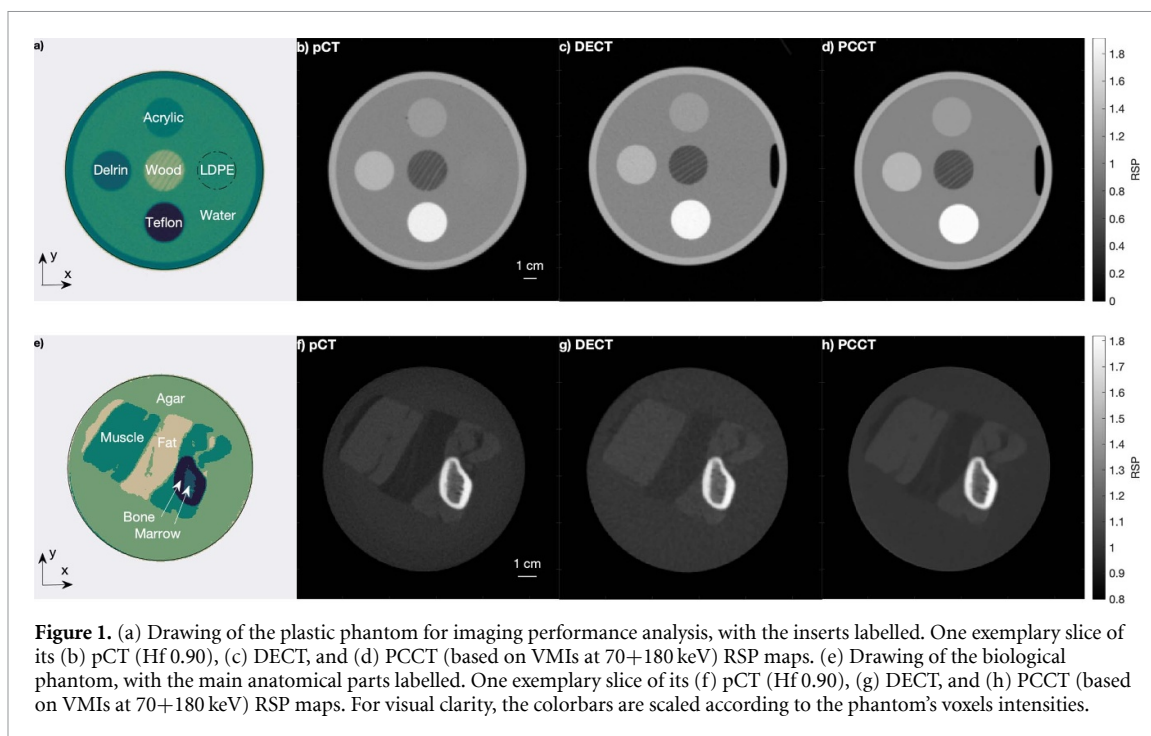


Table 2. Spatial resolution and noise of the three scanners. The $1\text{-}\sigma$ errors for the spatial resolution values are indicated in brackets.

	pCT (Hf 1.00)	pCT (Hf 0.90)	DECT	PCCT (70+180 keV)
Spatial resolution [lp/mm]	Teflon 0.56 (0.01)	0.55 (0.01)	0.538 (0.004)	0.546 (0.004)
	Delrin 0.55 (0.01)	0.54 (0.01)	0.542 (0.008)	0.544 (0.003)
	Acrylic 0.54 (0.03)	0.54 (0.02)	0.52 (0.03)	0.544 (0.006)
RSP Standard deviation	0.009	0.007	0.010	0.004

visible in the plastic phantom images (figures 1(b)–(d)). Note that a larger air bubble is visible in xCT images, due to the horizontal positioning of the phantom, as opposed to the vertical positioning for pCT acquisition. The LDPE insert is not distinguishable from the water background (figure 1(a), insert with dashed edge) due to the comparable RSP value to that of water (table 3). This makes estimating the spatial resolution associated with this insert non-trivial and therefore it is not included in this report.

More quantitatively, the spatial resolution and standard deviation of the three scanners are reported in table 2. The pCT performance is reported for the image reconstruction with the Hann filter with cut-off frequency 1.00 (Hf 1.00) and 0.90 (Hf 0.90). As expected, the latter shows a lower spatial resolution and a lower noise level. In particular, with Hf 0.90, the pCT spatial resolution is comparable both with the DECT images and with the PCCT images obtained with the energy couple 70+180 keV. Additionally, this PCCT energy couple results to be the least noisy compared to the others, as reported in figure 2.

In general, the DECT images are noisier than the PCCT ones at same dose level. A direct comparison with the pCT noise level is not feasible due to different dose values. The pCT noise is expected to decrease by increasing the dose level of the pCT images up to that of the xCTs. An estimation of the noise reduction as function of the dose is reported in supplementary materials (section 2) and suggests a potentially comparable noise level between the pCT and PCCT scanners at the same dose level. Nevertheless, it is evident that the pCT images exhibit a reduced level of noise in comparison to the DECT images. Furthermore, the pCT noise level diminishes through the reduction of the Hann filter cut-off frequency, aligning with findings from Fogazzi et al (2023).

3.2. RSP accuracy

The RSP accuracy of each insert is reported in table 3 for the three scanners. Moreover, for a clearer comparison among the three scanners, the RSP accuracy values are also displayed in a bar chart in figure 3. As for noise level, the energy couple 70+180 keV of PCCT images results to be the optimal one in terms of MAPE (figure 2). Therefore, this pair is considered the overall optimal in our study due to its reduced noise, best accuracy, and matching the spatial resolution of both the pCT and DECT scanners. Comparing the three

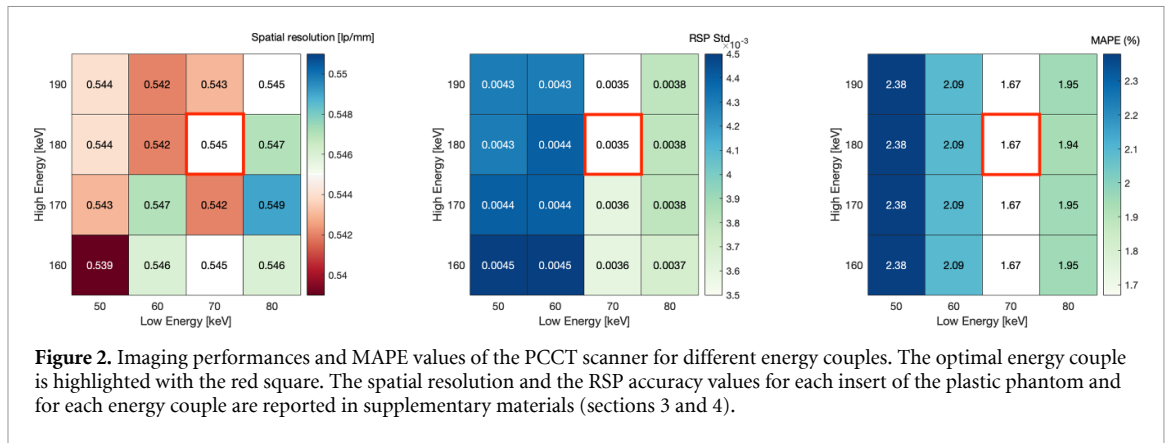


Figure 2. Imaging performances and MAPE values of the PCCT scanner for different energy couples. The optimal energy couple is highlighted with the red square. The spatial resolution and the RSP accuracy values for each insert of the plastic phantom and for each energy couple are reported in supplementary materials (sections 3 and 4).

Table 3. RSP accuracy and MAPE of the three scanners. The uncertainties on RSP accuracy values were calculated from error propagation.

Insert	RSP _{ref}	pCT (Hf 1.00) RSP _{acc} (%)	pCT (Hf 0.90) RSP _{acc} (%)	DECT RSP _{acc} (%)	PCCT (70+180 keV) RSP _{acc} (%)
Teflon	1.790 (0.003)	0.02 (0.17)	0.02 (0.17)	3.38 (0.17)	5.14 (0.18)
Delrin	1.352 (0.002)	-0.06 (0.15)	-0.06 (0.15)	0.13 (0.15)	1.26 (0.15)
Acrylic	1.157 (0.002)	0.06 (0.17)	0.06 (0.17)	0.25 (0.17)	0.44 (0.17)
LDPE	1.008 (0.002)	0.67 (0.20)	0.62 (0.20)	-1.35 (0.20)	-1.29 (0.20)
Water (21 °C)	0.998	-0.37 (0.01)	-0.37 (0.01)	0.30 (0.01)	0.201 (0.004)
MAPE (%)		0.23 (0.07)	0.22 (0.07)	1.20 (0.07)	1.67 (0.07)
MAPE without teflon (%)		0.29 (0.08)	0.28 (0.08)	0.51 (0.08)	0.80 (0.08)

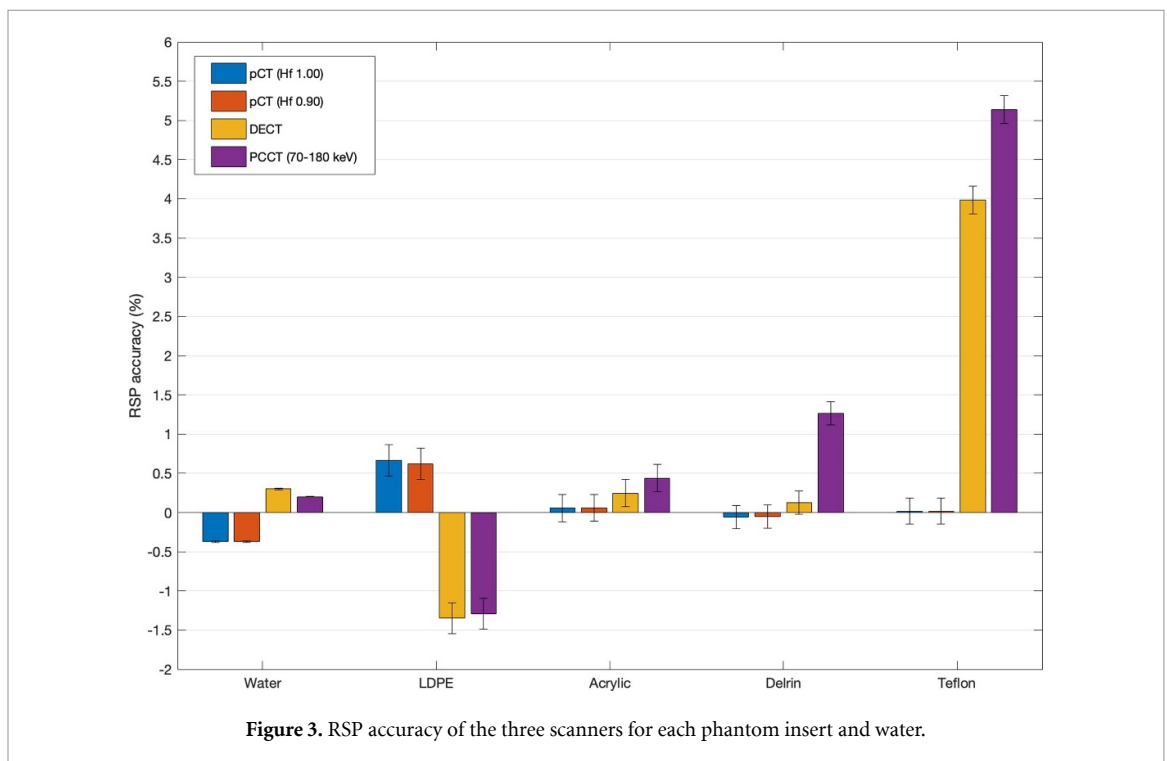


Figure 3. RSP accuracy of the three scanners for each phantom insert and water.

scanners, the lowest MAPE value is obtained with the pCT system (table 3). For both DECT and PCCT scanners, the RSP accuracy is below $\pm 1.30\%$ for all the inserts, except for the Teflon one, as expected. Indeed, the actual material composition of this plastic is expected to significantly diverge from the standard ICRU tissues composition, especially in terms of the fluorine content. Moreover, the xCT scanners were calibrated using tissue-equivalent materials distinct from Teflon (see section 2.1). Excluding the teflon insert, the MAPE of DECT and PCCT scanners is markedly reduced.

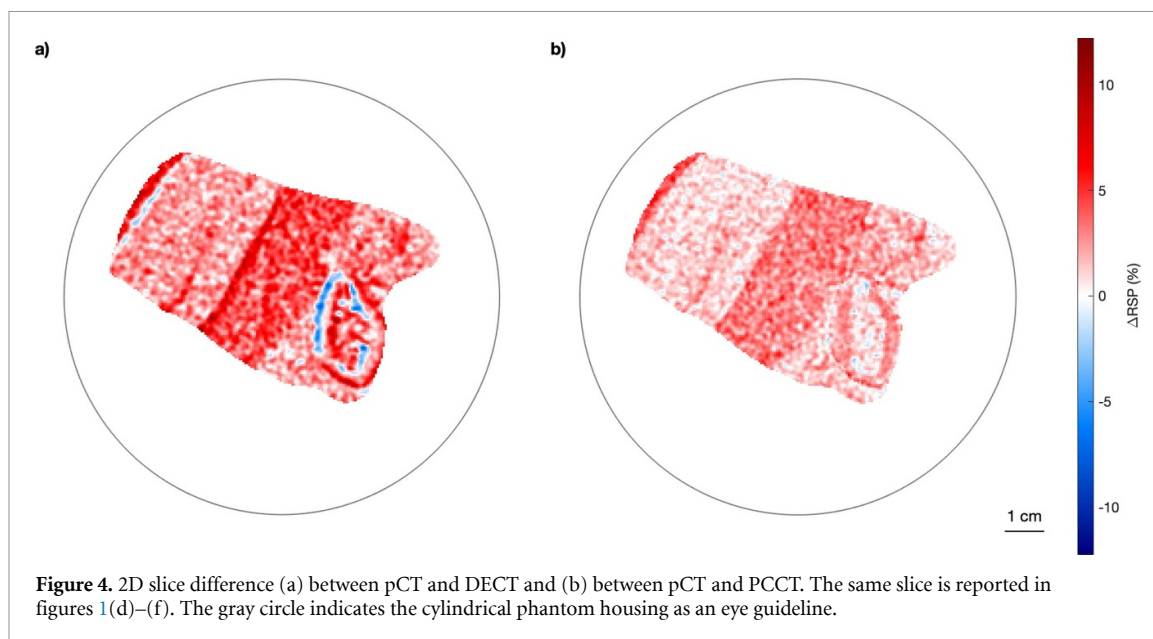


Table 4. Median, 5th and 95th percentiles of the Δ RSP distribution of fat, muscle, and bone, both for DECT and PCCT bio-phantom images. The uncertainties were derived through error propagation, taking into account the voxel count of the anatomical regions.

Tissue	xCT scanner	Δ RSP (%)		
		5th percentile	Median	95th percentile
Fat	DECT	2.21 (0.01)	4.42 (0.01)	6.85 (0.01)
	PCCT	1.27 (0.01)	2.98 (0.01)	4.77 (0.01)
Muscle	DECT	0.09 (0.01)	2.14 (0.01)	4.31 (0.01)
	PCCT	-0.48 (0.01)	1.14 (0.01)	2.91 (0.01)
Bone	DECT	-2.45 (0.05)	1.78 (0.05)	6.64 (0.05)
	PCCT	0.44 (0.02)	2.42 (0.02)	3.99 (0.02)

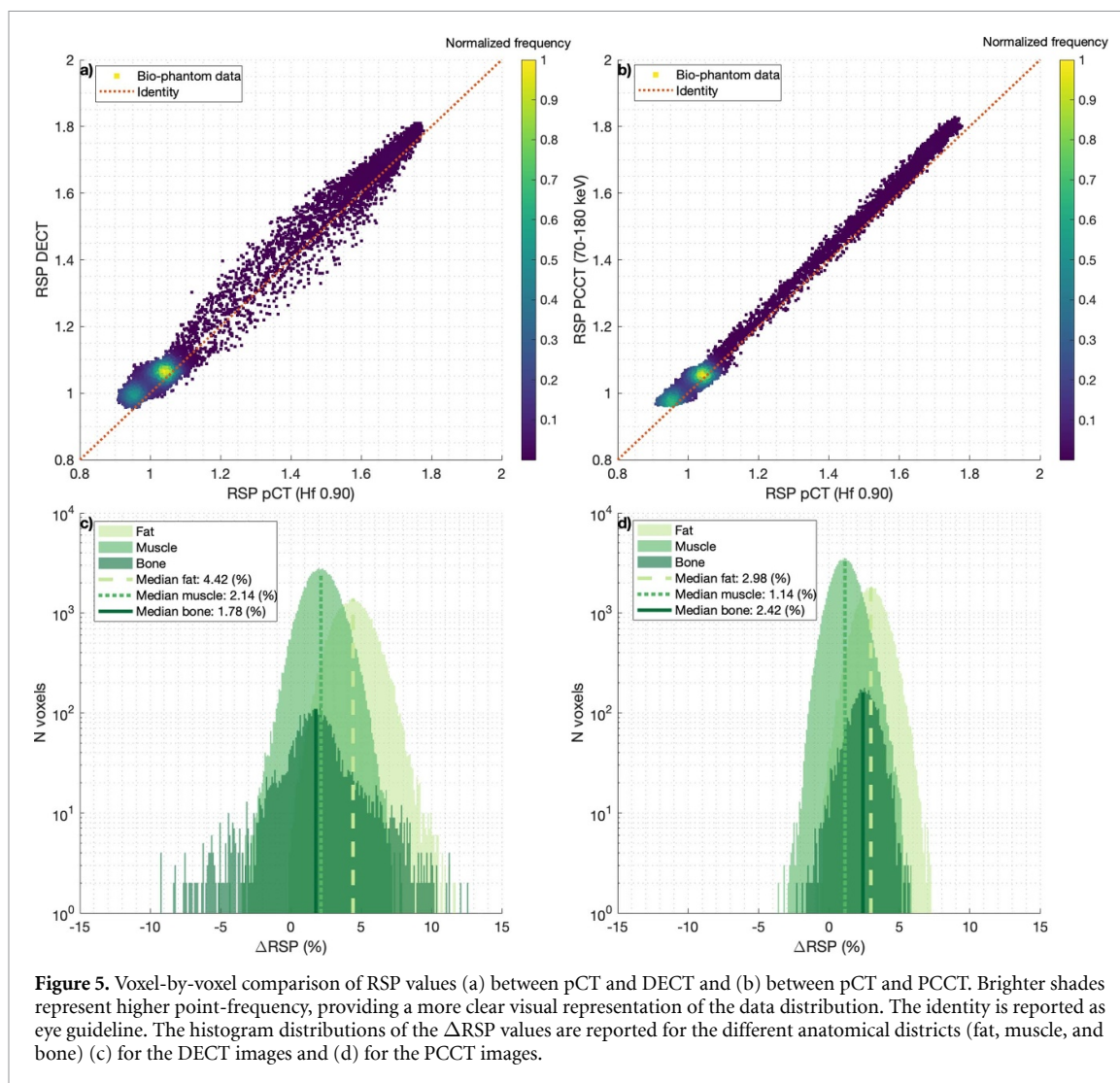
3.3. Bio-phantom RSP comparison

As first comparison of the bio-phantom RSP maps, an exemplary 2D slice difference is shown in figure 4. Only the optimal PCCT energy couple is shown. The xCT calibrations overestimate the RSP values in the vast majority of the pixels in comparison with the pCT image. The largest discrepancies appear in the DECT images, especially in the fat and bone regions (figure 4(a)). In particular, the fat portion is clearly distinguishable and exhibits high deviation values, even in the PCCT image (figure 4(b)). Furthermore, the substantial variations observed in the bone inner region are likely a result of its heterogeneity and cavities, leading to partial volume effects.

For a more complete analysis, the voxel-by-voxel comparison of the 3D maps is shown in figures 5(a) and (b), excluding the bone inner region. The spread of points further confirms the higher noise level of DECT images compared to PCCT ones. The most populated regions below an RSP of 1.2 are related to the fat and muscle regions, as further distinguished in the figures 5(c) and (d). Considering the median value of the histogram distributions, the largest discrepancy occurs in the fat region, both for DECT and PCCT images. This may be in part related to temperature conditions, as reported in the Discussion. The PCCT-based RSP values are more accurate than the DECT values in the muscle region. The opposite behaviour occurs in the bone region, considering the median value. However, it is worth noting that the Δ RSP (%) distribution related to the bone region is wider for DECT than PCCT, reaching absolute values above $\pm 4\%$ (table 4). This further confirms the higher noise level of DECT images detected with the NPS analysis (table 2).

4. Discussion

The uncertainties associated with converting CT images into RSP maps remain a limiting factor in fully exploiting the potential for precise and tailored dose distribution in proton therapy. In this context, research efforts are currently directed towards improving CT scanners and refining calibration techniques, alongside the development of high-quality proton CT prototypes. This study presents, to the best of our knowledge,



the first comparison of both the imaging performance and tissue RSP estimation among DECT, PCCT and pCT scanners, simultaneously.

In particular, the performance analysis reported in Fogazzi *et al* (2023) for pCT was extended to DECT and PCCT images, to examine spatial resolution, noise, and RSP accuracy through a custom plastic phantom. The spatial resolution analysis revealed a potentially comparable image quality across the three scanners, estimated to be around 0.54 lp/mm. However, it is important to mention that, if the distance between tracker planes in the pCT scanner is extended to match the scanning distances of conventional xCT scanners, there will be a corresponding reduction in spatial resolution (Krah *et al* 2018). Furthermore, (Fogazzi *et al* 2023) extensively examined the dependence of pCT's spatial resolution performance on filter and contrast conditions, including comparisons with other pCT prototypes. Examining the noise spectra of both x-ray scanners at equivalent dose levels revealed that the DECT images exhibited higher noise levels. A direct comparison with the noise of pCT images was not feasible due to the lower dose during acquisition. Nevertheless, findings from this study hinted a potential signal-to-noise ratio of pCT images comparable to that of PCCT (cf supplementary materials, section 2). It is important to highlight that the noise analysis was specifically carried out on homogeneous water slices, while prior studies indicated a potential increase of the pCT noise level with the heterogeneity of the target mainly primarily attributed to multiple Coulomb scattering (Dickmann *et al* 2019).

The image performance analysis was conducted for sixteen pairs of VMIs for the PCCT scanner, with the low energy ranging between 50 keV and 80 keV and the high energy ranging between 160 and 190 keV. These were chosen based on the optimal energy pair, 60 keV and 180 keV, identified for EAN and RSP estimation in a previous study on Gammex inserts (Hu *et al* 2022). Nevertheless, in our study performed on the plastic phantom, the optimal pair, 70 keV and 180 keV, was determined to be the one with lower noise levels and a

lower relative error in terms of RSP accuracy. Furthermore, it was found to be the pair exhibiting a comparable spatial resolution level in relation to DECT and pCT images.

Most importantly, the accuracy of the RSP values determined via CT number calibration and measured using pCT was evaluated against a reference value obtained through a multi-layer ionisation chamber measurement. The pCT offered the most accurate RSP estimation with a MAPE of $(0.28 \pm 0.07)\%$. Higher values were obtained with the DECT and PCCT images: $(0.51 \pm 0.08)\%$ and $(0.80 \pm 0.08)\%$, respectively. It is important to note that although the phantom insert materials are not tissue equivalent materials (TEMs), their composition and mass density are close to those of standard TEMs, except for Teflon. This latter is expected to lack tissue equivalence and may not be accurately characterised by the xCT calibration method. The accuracy results achieved in calculating the RSP value using DECT and PCCT calibrations on plastic phantoms (and also on biological phantoms, as detailed below) further validated the superiority of multi-energy xCT systems over conventional SECT calibration, in line with findings from other studies (Möhler *et al* 2016, 2018, Taasti *et al* 2017, 2018a, 2018b, Wohlfahrt *et al* 2017, Xie *et al* 2018, Dedes *et al* 2019, Niepel *et al* 2021). Indeed, employing diverse energy spectra enables the estimation of RED and EAN of materials from CT images. This effectively eliminates the degeneracy between CT number and RSP values, which is a notable limitation of conventional SECT calibrations. Such advancements provide further rationale for the growing interest and efforts to implement these systems in clinical settings.

Moving toward more clinical targets, a stabilised biological phantom was scanned with the three imaging systems. This enabled a comparison of the RSP values of real biological tissues such as fat, muscle, and bone. A reference measurement of the bio-phantom RSP values was not conducted with the multi-layer ionisation chamber, as was done for the plastic phantom, due to the heterogeneity and complexity of the phantom. Previous studies have focused on homogenised tissues, which lacks in accurately mimicking the response of complex, heterogeneous targets (Möhler *et al* 2018, Bär *et al* 2022). Additionally, investigations have been performed on 1D (i.e. proton range) or 2D (i.e. proton radiography) information on heterogeneous samples (Xie *et al* 2018, Meijers *et al* 2020, DeJongh *et al* 2021a). However, a pCT system has the potential to address these limitations by directly measuring the 3D RSP map of heterogeneous targets. The potential of this novel procedure—that is, pCT of a heterogeneous biological phantom—has been introduced in Fogazzi *et al* (2024) for SECT calibrations and was adapted for multi-energy CT scanners in this study.

Comparing the tissue RSP values obtained with the DECT and PCCT with respect to pCT, notable differences were observed, especially in fat tissues. The median RSP relative difference values in fat regions were about 4.42% and 2.98% for DECT and PCCT, respectively. Conversely, the disparities were lower (below 2.50%) in the muscle and bone regions. This divergence may be partially attributed to different temperature conditions between xCT and pCT acquisitions. Research into the temperature effects on CT numbers of biological tissues suggested that this influence may be significant, particularly for fat tissues (Fogazzi *et al* 2024). A similar dependency may be expected for RSP values. Supplementary materials (section 5) provide a potential quantification of this effect, estimating for the fat tissue an RSP relative difference in the range $[1.32, 4.21]\%$ for the scanning temperature conditions of this study. However, since the temperature control during xCT acquisition was not fully regulated, accurately quantifying this effect may be challenging. Consequently, temperature effects could jeopardise a proper one-to-one comparison of RSP values, particularly in fat tissues. Measurements under a controlled temperature environment are foreseen to elucidate this phenomenon and possible effects will be discussed in detail in forthcoming works.

Nevertheless, this study, alongside investigations outlined in Fogazzi *et al* (2024), represents a crucial preliminary exploration of utilising such a novel phantom for a wider inter-centre comparison of the accuracy and variability of CT-number-to-RSP calibration methods, using the proton CT as reference imaging tool.

5. Conclusions

In this study, an experimental assessment was conducted to evaluate imaging performance and estimate tissue RSP using two multi-energy x-ray CT scanners and a proton CT prototype. Analysis of plastic materials indicated that proton CT might provide superior accuracy in RSP estimation. These findings suggested the potential usefulness of proton CT as a benchmark measurement for validating x-ray CT calibration accuracy on heterogeneous biological phantoms. This first trial with biological phantoms underscored both the possible benefits and constraints for wider inter-centre surveys in future.

Data availability statement

The data cannot be made publicly available upon publication because no suitable repository exists for hosting data in this field of study. The data that support the findings of this study are available upon reasonable request from the authors.









Acknowledgment

Work supported by the Italian National Institute of Nuclear Physics (INFN, experiment XpCalib-CSN5), German Research Foundation (Research Training Group GRK2274), and Bavarian High-Tech Agenda (project EQAP).

Conflict of interest

Nothing to declare.

ORCID iDs

Elena Fogazzi  <https://orcid.org/0000-0002-2527-4070>
Guyue Hu  <https://orcid.org/0009-0004-0821-7236>
Paolo Farace  <https://orcid.org/0000-0002-6051-2345>
Monica Scaringella  <https://orcid.org/0000-0002-6753-2832>
Francesco Tommasino  <https://orcid.org/0000-0002-8684-9261>
Guillaume Landry  <https://orcid.org/0000-0003-1707-4068>
Carlo Civinini  <https://orcid.org/0000-0002-4952-3799>
Katia Parodi  <https://orcid.org/0000-0001-7779-6690>

References

- Bär E, Volz L, Collins-Fekete C-A, Brons S, Runz A, Schulte R W and Seco J 2022 Experimental comparison of photon versus particle computed tomography to predict tissue relative stopping powers *Med. Phys.* **49** 474–87
- Civinini C et al 2017 Proton computed tomography: iterative image reconstruction and dose evaluation *J. Instrum.* **12** C01034
- Civinini C, Scaringella M, Brianzi M, Intravaia M, Randazzo N, Sipala V, Rovituso M, Tommasino F, Schwarz M and Bruzzi M 2020 Relative stopping power measurements, prosthesis artifacts reduction in proton CT *Phys. Med. Biol.* **65** 225012
- Dedes G et al 2019 Experimental comparison of proton CT and dual energy x-ray CT for relative stopping power estimation in proton therapy *Phys. Med. Biol.* **64** 165002
- Dedes G et al 2022 Comparative accuracy and resolution assessment of two prototype proton computed tomography scanners *Med. Phys.* **49** 4671–81
- DeJongh D F et al 2021 A comparison of proton stopping power measured with proton CT and x-ray CT in fresh postmortem porcine structures *Med. Phys.* **48** 7998–8009
- DeJongh E A et al 2021 Technical note: a fast and monolithic prototype clinical proton radiography system optimized for pencil beam scanning *Med. Phys.* **48** 1356–64
- Dickmann J et al 2019 Prediction of image noise contributions in proton computed tomography and comparison to measurements *Phys. Med. Biol.* **64** 145016
- Dobbins III J T 2000 Image quality metrics for digital systems *Handbook of Medical Imaging, Vol. I: Physics and Psychophysics* ed J Beutel, H L Kundel and R L Van Metter (SPIE)
- Esposito M et al 2018 Pravda: the first solid-state system for proton computed tomography *Phys. Med.* **55** 149–54
- Farace P, Tommasino F, Righetto R, Fracchiolla F, Scaringella M, Bruzzi M and Civinini C 2021 Technical note: CT calibration for proton treatment planning by cross-calibration with proton CT data *Med. Phys.* **48** 1349–55
- Fogazzi E, Bruzzi M, D'amato E, Farace P, Righetto R, Scaringella M, Scarpa M, Tommasino F and Civinini C 2024 Proton CT on biological phantoms for x-ray CT calibration in proton treatment planning *Phys. Med. Biol.* **69** 135009
- Fogazzi E, Trevisan D, Farace P, Righetto R, Rit S, Scaringella M, Bruzzi M, Tommasino F and Civinini C 2023 Characterization of the INFN proton CT scanner for cross-calibration of x-ray CT *Phys. Med. Biol.* **68** 124001
- Hu G, Niepel K, Risch F, Kurz C, Würll M, Kröncke T, Schwarz F, Parodi K and Landry G 2022 Assessment of quantitative information for radiation therapy at a first-generation clinical photon-counting computed tomography scanner *Front. Oncol.* **12** 970299
- Hudobivnik N et al 2016 Comparison of proton therapy treatment planning for head tumors with a pencil beam algorithm on dual and single energy CT images *Med. Phys.* **43** 495
- Johnson R P et al 2016 A fast experimental scanner for proton CT: technical performance and first experience with phantom scans *IEEE Trans. Nucl. Sci.* **63** 52–60
- Krah N, Khellaf F, Létang J M, Rit S and Rinaldi I 2018 A comprehensive theoretical comparison of proton imaging set-ups in terms of spatial resolution *Phys. Med. Biol.* **63** 135013
- Li B, Lee H C, Duan X, Shen C, Zhou L, Jia X and Yang M 2017 Comprehensive analysis of proton range uncertainties related to stopping-power-ratio estimation using dual-energy CT imaging *Phys. Med. Biol.* **62** 7056
- Meijers A, Free J, Wagenaar D, Deffet S, Knopf A C, Langendijk J A and Both S 2020 Validation of the proton range accuracy and optimization of ct calibration curves utilizing range probing *Phys. Med. Biol.* **65** 03NT02
- Möhler C, Russ T, Wohlfahrt P, Elter A, Runz A, Richter C and Greulich S 2018 Experimental verification of stopping-power prediction from single- and dual-energy computed tomography in biological tissues *Phys. Med. Biol.* **63** 025001

- Möhler C, Wohlfahrt P, Richter C and Greulich S 2016 Range prediction for tissue mixtures based on dual-energy CT *Phys. Med. Biol.* **61** N268–75
- Niepel K B *et al* 2021 Animal tissue-based quantitative comparison of dual-energy CT to SPR conversion methods using high-resolution gel dosimetry *Phys. Med. Biol.* **66** 075009
- NIST-Physical Measurement Laboratory. 2023 Pstar-stopping-power and range tables for proton (available at: <https://physics.nist.gov/PhysRefData/Star/Text/PSTAR.html>)
- Peters N *et al* 2023 Consensus guide on CT-based prediction of stopping-power ratio using a hounsfield look-up table for proton therapy *Radiother. Oncol.* **184** 109675
- Petersen H E S *et al* 2017 Proton tracking in a high-granularity digital tracking calorimeter for proton CT purposes *Nucl. Instrum. Methods Phys. Res. A* **860** 51–61
- Rit S, Dedes G, Freud N, Sarrut D and Létang J 2013 Filtered backprojection proton ct reconstruction along most likely paths *Med. Phys.* **40** 031103
- Saito M 2012 Potential of dual-energy subtraction for converting CT numbers to electron density based on a single linear relationship *Med. Phys.* **39** 2021–30
- Saito M and Sagara S 2017 A simple formulation for deriving effective atomic numbers via electron density from dual-energy CT data in the human body *Med. Phys.* **44** 2293–303
- Saito M and Sagara S 2017 Simplified derivation of stopping power ratio in the human body from dual-energy CT data *Med. Phys.* **44** 4179–87
- Samei E *et al* 2019 Performance evaluation of computed tomography systems: summary of AAPM task group 233 *Med. Phys.* **46** e735–56
- Scaringella M, Bruzzi M, Farace P, Fogazzi E, Righetto R, Rit S, Tommasino F, Verroi E and Civinini C 2023 The infn proton computed tomography system for relative stopping power measurements: calibration, verification *Phys. Med. Biol.* **68** 154001
- Schaffner B and Pedroni E 1998 The precision of proton range calculations in proton radiotherapy treatment planning: experimental verification of the relation between CT-HU and proton stopping power *Phys. Med. Biol.* **43** 1579
- Schneider U, Pedroni E and Lomax A 1996 The calibration of CT hounsfield units for radiotherapy treatment planning *Phys. Med. Biol.* **41** 111–24
- Schulte R W, Penfold S N, Tafas J T and Schubert K E 2008 A maximum likelihood proton path formalism for application in proton computed tomography *Med. Phys.* **35** 4849–56
- Seltzer S M, Fernandez-Varea J M, Andreo P, Bergstrom P M J, Burns D T, Krajcar Bronic I, Ross C K and Salvat F 2014 Report 90: key data for ionizing-radiation dosimetry: measurement standards and applications *J. ICRU* **14** 11–110
- Shen C, Li B, Chen L, Yang M, Lou Y and Jia X 2018 Material elemental decomposition in dual and multi-energy CT via a sparsity-dictionary approach for proton stopping power ratio calculation *Med. Phys.* **45** 1491–503
- Si-Mohamed S, Bar-Ness D, Sigovan M, Cormode D P, Coulon P, Coche E, Vlassenbroek A, Normand G, Bousset L and Douek P 2017 Review of an initial experience with an experimental spectral photon-counting computed tomography system *Nucl. Instrum. Methods Phys. Res. A* **873** 27–35
- Sigmund P, Schinner A and Paul H 2009 Errata and addenda for ICRU report 73, stopping of ions heavier than helium *ICRU J.* **5** 113–237
- Taasti V T, Hansen D C, Michalak G J, Deisher A J, Kruse J J, Muren L P, Petersen J B B and McCollough C H 2018 Theoretical and experimental analysis of photon counting detector CT for proton stopping power prediction *Med. Phys.* **45** 5186–96
- Taasti V T, Michalak G J, Hansen D C, Deisher A J, Kruse J J, Krauss B, Muren L P, Petersen J B B and McCollough C H 2017 Validation of proton stopping power ratio estimation based on dual energy CT using fresh tissue samples *Phys. Med. Biol.* **63** 015012
- Taasti V T, Muren L P, Jensen K, Petersen J B B, Thygesen J, Tietze A, Grau C and Hansen D C 2018 Comparison of single and dual energy CT for stopping power determination in proton therapy of head and neck cancer *Phys. Imaging Radiat. Oncol.* **6** 14–19
- Tommasino F *et al* 2017 Proton beam characterization in the experimental room of the trento proton therapy facility *Nucl. Instrum. Methods Phys. Res. A* **869** 15–20
- Willemink M J, Persson M, Pourmorteza A, Pelc N J and Fleischmann D 2018 Photon-counting CT: technical principles and clinical prospects *Radiology* **289** 293–312
- Wohlfahrt P, Möhler C, Hietschold V, Menkel S, Greulich S, Krause M, Baumann M, Enghardt W and Richter C 2017 Clinical implementation of dual-energy CT for proton treatment planning on pseudo-monoenergetic CT scans *Int. J. Radiat. Oncol. Biol. Phys.* **97** 427–34
- Wohlfahrt P and Richter C 2020 Status and innovations in pre-treatment CT imaging for proton therapy *Br. J. Radiol.* **93** 20190590
- Woodard H Q and White D R 1986 The composition of body tissues *Br. J. Radiol.* **59** 1209–18
- Xie Y, Ainsley C, Yin L, Zou W, McDonough J, Solberg T D, Lin A and Teo B-K K 2018 Ex vivo validation of a stoichiometric dual energy CT proton stopping power ratio calibration *Phys. Med. Biol.* **63** 055016
- Yang M, Zhu X R, Park P C, Titt U, Mohan R, Virshup G, Clayton J E and Dong L 2012 Comprehensive analysis of proton range uncertainties related to patient stopping-power-ratio estimation using the stoichiometric calibration *Phys. Med. Biol.* **57** 4095–115